Research Article | Vol. 31, No. 15 / 17 Jul 2023 / Optics Express 24142
Optics EXPRESS

High-energy parametric oscillator and amplifier pulsed light source at 2-µm

LARS BEHNKE,[1,2] EDCEL J. SALUMBIDES,[1] GUIDO GÖRITZ,[3] YAHIA MOSTAFA,[1,2] DION ENGELS,[1,2] WIM UBACHS,[1,2] AND OSCAR VERSOLATO[1,2,*]

[1]*Advanced Research Center for Nanolithography (ARCNL), Science Park 106, 1098 XG Amsterdam, The Netherlands*
[2]*Department of Physics and Astronomy and LaserLab, Vrije Universiteit Amsterdam, De Boelelaan 1081, 1081 HV Amsterdam, The Netherlands*
[3]*GWU-Lasertechnik GmbH, Bonner-Ring 9, 50374 Erftstadt, Germany*
[*]*versolato@arcnl.nl*

Abstract: A laser system generating high-energy pulses at 2-µm wavelength with pulse widths tunable from 10–24 ns is described. It comprises an optical parametric oscillator that generates mJ-level signal seed radiation and an optical parametric amplifier that boosts the output to 800 mJ of combined signal and idler when pumped with 2 J pulses of 1064-nm laser light. The system operated with KTP crystals and running at 10 Hz repetition rate is characterized in the spatial, temporal, and spectral domains. The effect of saturation leads to an output pulse approaching flat-top spatial and box-shaped temporal profiles, as desired in various applications. The amplified pulses can be imaged down to sub-100 µm diameters, making this laser system a suitable driver for plasma sources of extreme ultraviolet light.

1. Introduction

Mid-infrared (MIR) laser sources are of interest in various applications, including spectroscopy [1], laser ranging (LIDAR) [2], medical applications [3], material processing [4], and defense [4]. These applications require continuous-wave to ultra-fast pulsed sources [5,6]. High-energy laser sources of nanosecond pulses at 2–10 µm radiation are of particular interest for extreme ultraviolet (EUV) light generation in EUV lithography [7]. Here, pulses of several hundred mJ are imaged onto tin targets to create EUV emitting plasma. A full geometrical overlap of laser profile and target is crucial to obtain the highest conversion efficiencies of laser pulse energy to EUV radiation [8]. This case poses an example of an application requiring high pulse energies with good spatial and temporal beam characteristics.

Possible sources at 2-µm wavelength fulfilling the aforementioned criteria are Tm^{3+}/Ho^{3+}-doped solid-state and fiber lasers [5]. An example is the high-energy Big Aperture Thulium (BAT) laser system operating at 1.9 µm-wavelength [9,10]. This laser has been demonstrated to provide an output of several 10 joules per pulse [11,12], albeit at a low repetition rate.

Alternatively, optical parametric oscillators (OPOs) can be used to generate MIR laser light based on non-linear wave mixing. Nanosecond OPOs generating several hundred mJ/pulse have been built [13,14], but combining high energy, high efficiency, and good beam quality remains a challenge [15]. Arisholm et al. [16] give an overview of the main challenges of combining high pulse energies in OPOs and good beam quality. High-energy OPO designs are limited by the achievable build-up time, which is the characteristic time required for amplifying the signal beam from quantum noise to significant pulse energies. The build-up time needs to be short compared to the duration of the pump pulse to obtain a high overall efficiency because only after the build-up time is efficient amplification of the signal beam possible. Since laser pulse durations of high-power pump lasers are usually in the order of nanoseconds, it is crucial to limit

#494082 https://doi.org/10.1364/OE.494082
Journal © 2023 Received 25 Apr 2023; revised 21 Jun 2023; accepted 21 Jun 2023; published 7 Jul 2023

Optics EXPRESS

the build-up time to values well below that. This constraint limits possible resonator designs, particularly regarding the maximum resonator length, that would enable more transverse-mode control for beam quality enhancement. There are many approaches to enhance beam quality, such as unstable confocal resonators [17–21] and image-rotating resonator designs [15,22,23]. However, these approaches tend to increase the build-up time [16]. Lowering the transverse mode count in the resonator by reducing the pump beam diameter would lead (at constant energy) to exceeding the damage thresholds of the non-linear crystals and other optics, resulting in a trade-off between pulse energy and beam quality.

These limitations can be overcome by implementing a master oscillator and power amplifier (MOPA) architecture [16,24,25]. In such a configuration, an OPO acts as the master oscillator creating a seed beam at relatively low pulse energies with a reduced beam diameter, thus suppressing higher transversal modes. The OPO output beam is expanded and used to seed an optical parametric amplifier (OPA) boosting the output energy of the combined system. This design enables the generation of several hundred mJ pulse energy at high spatio-temporal beam quality because the OPA does not allow additional modes to grow.

The parametric MOPA introduced by Arisholm et al. delivered close to 300 mJ of total pulse energy (signal and idler combined) at a pulse duration of 6 ns [16]. With our present laser design, similarly based on KTP crystals, we demonstrate the generation of 2 µm-wavelength laser light with more than twice the pulse energy, and with variable pulse durations including temporal shaping. The quality of the output beam supports the demagnification of a flat-top spatial beam profile by a factor of 75, to below a spot diameter of 100 µm. We designed the MOPA for driving EUV-emitting laser-produced plasma (LPP), and successfully used it to demonstrate tin-plasmas driven by a 2-µm laser wavelength [7,26,27]. In this publication, we report on an extensive characterization of our high-energy 2-µm MOPA system.

2. Experimental setup

A schematic of the laser system is shown in Fig. 1. The upper panel shows the master oscillator power amplifier (MOPA), with an OPO stage whose output is used for seeding a 4-crystal OPA amplification stage. The lower panel shows light transportation and a high numerical aperture imaging system used to project the flat-top beam profile onto tin microdroplets in a vacuum chamber as part of a typical application in laser-produced, EUV-emitting plasmas at ARCNL. The two stages are indicated by their respective frames.

The MOPA configuration generates high pulse energies at 2-µm wavelengths with high beam quality following the design of Arisholm et al. [16]. An injection-seeded Nd:YAG laser (Amplitude Agilite, referred to as pump laser), emitting pulses at a wavelength of 1064 nm and repetition rate of 10 Hz, pumps the MOPA. This pump laser has advanced temporal pulse shaping capabilities, here allowing the laser pulse durations to be varied between 10 ns and 27 ns by means of a Pockels cell, such that the pump laser peak power remains constant. Accordingly, the attainable pulse energies scale with the set pulse duration ranging from 2.3 J at 27 ns to 0.9 J at 10 ns. The pump laser beam is split using a polarizing beam splitter to provide a small fraction (<80 mJ) for pumping the optical parametric oscillator, while most of the pump energy is delivered to the optical parametric amplification stage.

Our OPO (a customized version of GWU versaScan-L 1064) has a 30-mm-length linear cavity comprised of flat dichroic resonator mirrors that are designed for single-pass pumping, so they are highly transmissive for the 1064-nm pump. The optical cavity resonates the signal wavelengths (i.e., wavelengths shorter than degeneracy at 2128 nm), and a fraction of the signal pulse energy being transmitted through the output coupler (CM2 in Fig. 1). The OPO contains a single KTP (potassium titanyl phosphate) crystal of 18.2 mm length and with an aperture of 15×13 mm^2. The crystal surfaces are anti-reflection coated for the 1064-nm pump wavelength and any wavelength generated in the range around 2 µm. A pump pulse energy of 76 mJ (at 27 ns) is used for pumping

Optics EXPRESS

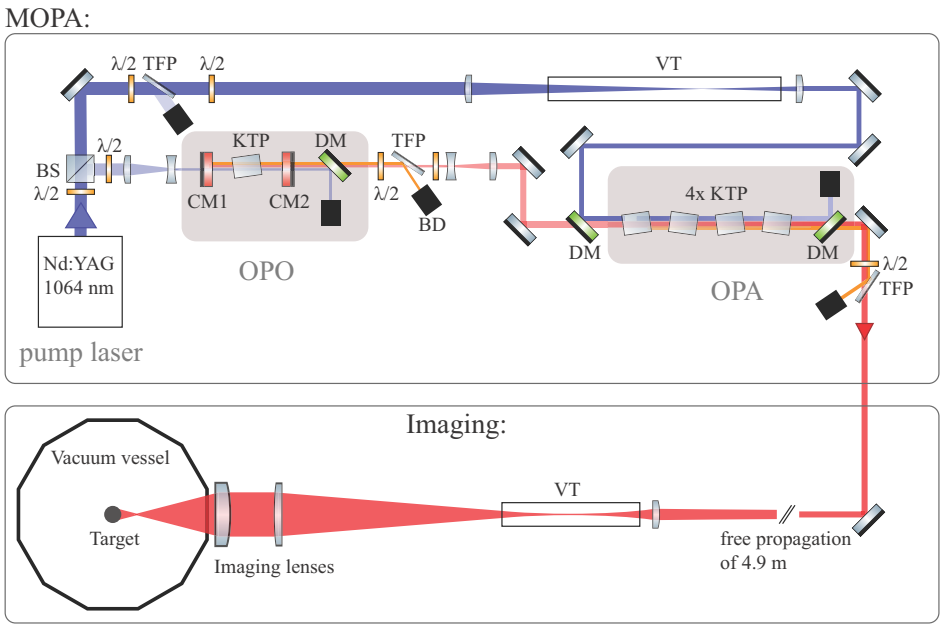

Fig. 1. Schematic representation of the MOPA. The oscillator (OPO) and amplifier (OPA) are pumped by a Nd:YAG laser (pump laser) operating at 1064 nm wavelengths. The wavelengths generated are 2090 nm and 2167 nm. The flat-top beam profile of the MOPA output can be imaged onto a target with a 75-times reduction in size. ($\lambda/2$: half-wave plate, BS: polarizing beam splitter, TFP: thin-film polarizer, BD: beam dump, CM1 and CM2: cavity mirrors, DM: Dichroic mirror (reflection of 1064 nm, transmission of 2 µm wavelengths), KTP: Potassium titanyl phosphate (non-linear crystal for wave mixing), VT: vacuum tube).

the OPO. The beam diameter is reduced with a Galilean-type telescope to 2 mm in front of the OPO resonator. This small beam diameter is chosen to improve the beam quality of the generated 2-µm laser light [16]. The crystal angle is tuned to an angle of θ =50.8° to achieve type II phase matching (oe-o) for a signal around 2090 nm and corresponding idler around 2167 nm wavelength. While the pump is linearly polarized vertically (defined as being perpendicular to the plane of Fig. 1), the signal has horizontal and the idler vertical polarization. The output pulse energy of the signal is 3 mJ with a pulse duration of 21 ns. A dichroic mirror is used to separate the unconverted 1064-nm pump transmitted through the cavity from 2-µm light that propagates further. The OPO output characteristics are discussed in section 3.

After the OPO, the signal beam is further separated from the idler by means of a polarizing filter. A Galilean-type telescope is used to magnify the beam diameter of the signal to approximately 5×2 mm^2 to seed the OPA at an intensity of 2 MW/cm^2. The OPA consists of four identical KTP crystals with a crystal length of 18.2 mm and an aperture of 15×13 mm^2 each. We use four crystals to obtain a pulse energy up to 800 mJ of combined signal and idler. Similarly to the OPO, the crystal surfaces have antireflective coatings for the pump wavelength and wavelengths in the 2-µm range. The crystal angle is tuned to θ =50.8° for type II phase matching (oe-o) to amplify the 2090 nm wavelength seed light. Here, the seed at the signal wavelength has horizontal polarization, and the pump is vertically polarized. For pumping the OPA, most of the 2.2 J (at 27 ns) of pump laser output is used. The beam is transported via relay imaging to ensure a flat-top spatial beam profile of the pump within the OPA. Additionally, the pump beam is optically delayed by 4 ns to account for the build-up time of the OPO. To achieve sufficient

Optics EXPRESS

pump intensity within the OPA, its beam diameter is reduced from 12 mm to 6.5 mm, resulting in an intensity of approximately 220 MW/cm^2. The pump and seed beam are spatially overlapped using a dichroic mirror and aligned for propagation through the four crystals. The crystals are oriented for walk-off compensation (see Fig. 1). After the last crystal, the amplified 2-µm light and the remaining pump light are again separated by a dichroic mirror.

The MOPA is designed to drive LPPs at 2-µm wavelength. For this intended use, it is necessary to image and demagnify the flat-top beam profile onto a target as shown in the lower frame in Fig. 1. Flat-top imaged beams provide uniform heating of the LPP across the plasma surface at sufficiently high plasma temperatures, as was shown in the case of 1-µm wavelength-driven EUV emitting plasmas [8]. In this work, the output of the MOPA is imaged using a two-stage imaging setup. After a free propagation of about 4.9 m, the beam is imaged by a first spherical lens with a focal length of 400 mm (f400 mm). The intermediate image is reduced by about 11 times compared to the initial output beam diameter of the MOPA. After the intermediate image, the diverging beam is collimated with an f1000 mm lens. Subsequently, an f250 mm aspherical lens is used for imaging the beam onto a tin target. The total beam size reduction factor is up to 75 (chosen for a particular target size). Imaging the beam down to sub-100 µm diameters is possible due to a relatively low full beam divergence θ of approximately 2 mrad in the horizontal and 3 mrad in the vertical direction. Taking into account the waist diameter ω of the beam of approximately 5 mm, this leads to an M^2 value of $M_x^2 \approx 4$ along the horizontal axis and $M_y^2 \approx 6$ along the vertical axis following the relation $M^2 = \theta\pi\omega/(4\lambda)$ based on the beam parameter product with a wavelength of $\lambda = 2090$ nm. The characterization of the MOPA in terms of input and output energies, temporal beam profiles, and spatial profiles of the pump, signal, and idler beams are discussed in section 4.

3. Optical parametric oscillator

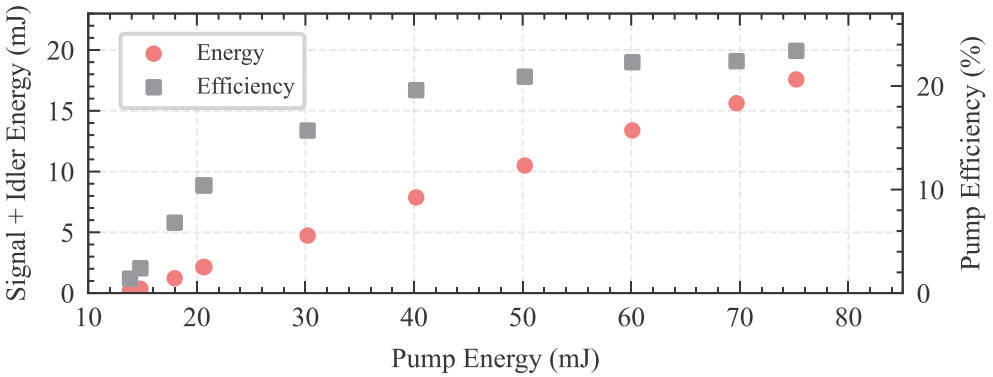

Fig. 2. Combined signal and idler energies from the OPO as a function of the input pump energy (for a box-shaped pump pulse of duration $\tau_p = 27$ ns). The corresponding efficiency for conversion summed over both signal and idler is also indicated. Error bars are smaller than the markers.

In this section, we discuss the characterization of the optical parametric oscillator including measurements on energy conversion, as well as recordings in the temporal domain. A representative graph in Fig. 2 shows the combined signal and idler OPO output energy as the input pump energy is varied. The conversion efficiency increases with pump energy, where pumping is limited below 80 mJ to avoid optical damage to cavity mirror coatings. Conversion to total output energies can reach efficiencies up to 24% (corresponding to a signal conversion efficiency of 12%) and shows a plateau indicating saturation at higher pumping energies. The pulse energy

Optics EXPRESS

of the combined signal and idler, obtained for the highest pump energy of 76 mJ, is 17 mJ with a root-mean-square (RMS) stability of approximately 2% (for comparison, the pump RMS stability is 1%). For decreased input pump energies, the lower conversion efficiencies should in part be attributed to the long cavity build-up time of the signal (and idler).

Temporal profiles were recorded using fast photodiodes (EOT ET-5000, 12-GHz bandwidth) and a fast oscilloscope (Agilent Technologies DSO9404A, 4-GHz bandwidth), with a typical recording shown in Fig. 3. Dichroic mirrors and optical filters separate the signal beam from the idler and pump beams. At a pump energy of 76 mJ, and pump pulse duration of $\tau_p = 27$ ns, the signal resembles a box-shaped pulse with a full-width-at-half-maximum (FWHM) duration that is shorter ($\tau_s = 21$ ns) than the pump. The build-up time τ_{bu} is defined as the delay between the onset of the signal and the pump pulse.

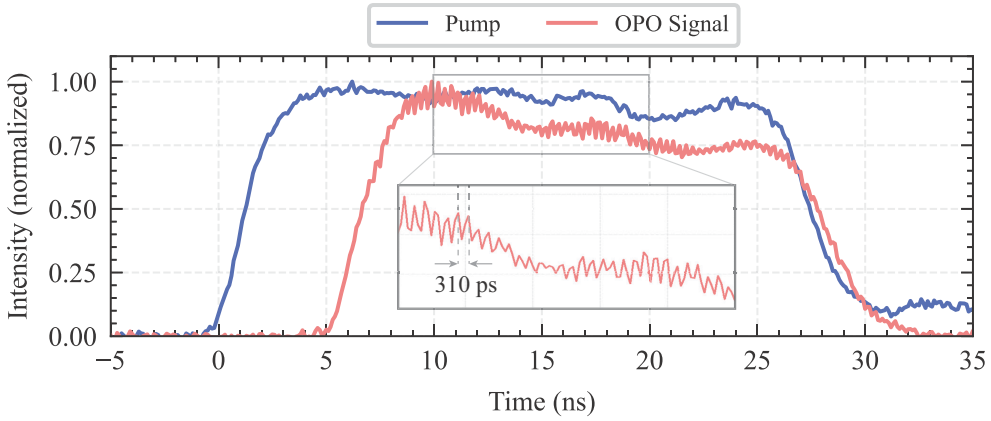

Fig. 3. OPO oscilloscope traces for a 27 ns FWHM pump pulse duration at maximum OPO pump pulse energy. The temporal profiles of the initial pump beam (blue) and the generated signal beam (red) are shown for a pump energy of 76 mJ/pulse. The FWHM pulse duration of the signal is 21 ns revealing a build-up time of about 5.5 ns. The inset figure shows a magnified signal trace in the 10–20 ns interval highlighting the beating due to competing longitudinal modes. A beating period of 310 ps is measured, closely matching the cavity round time of 300 ps.

Cavity build-up times for the OPO signal were measured for varying pump input energies as shown in Fig. 4. For a pump pulse with duration $\tau_p = 27$ ns, signal pulse durations of $\tau_s = 5 - 21$ ns were observed for the pump energy range covered. In addition to decreasing the signal energies and longer build-up times, the signal temporal profiles are found to increasingly deviate from a box-shaped profile and tend towards a Gaussian profile at decreasing pump energies.

The cavity-build up time τ_{bu} behavior in Fig. 4 can be approximated following the relations from Refs. [16,28], which can be expressed as:

$$\tau_{bu} = \frac{\tau_{cav}\ g_{Log}}{\sqrt{E_p/E_{th}} - \epsilon}, \tag{1}$$

where τ_{cav} is the resonator roundtrip time, g_{Log} is related to photodetector sensitivity, ϵ contains information on the effective reflectivity and other optical losses and is of order unity, E_p is the input pump energy and E_{th} is a pump threshold energy directly related to the characteristic nonlinear threshold intensity I_{th}. The cavity roundtrip time is estimated to be approximately 300 ps based on the KTP crystal length and cavity mirror separation. The fitted curve, displayed in Fig. 4, describes the experimental trend to sufficient accuracy. The fit yields $g_{Log} = 22$, which is close to $g_{Log} = \ln(I_{det}/I_{noise}) \approx 18$ that is the value commonly used in numerical studies

Optics EXPRESS

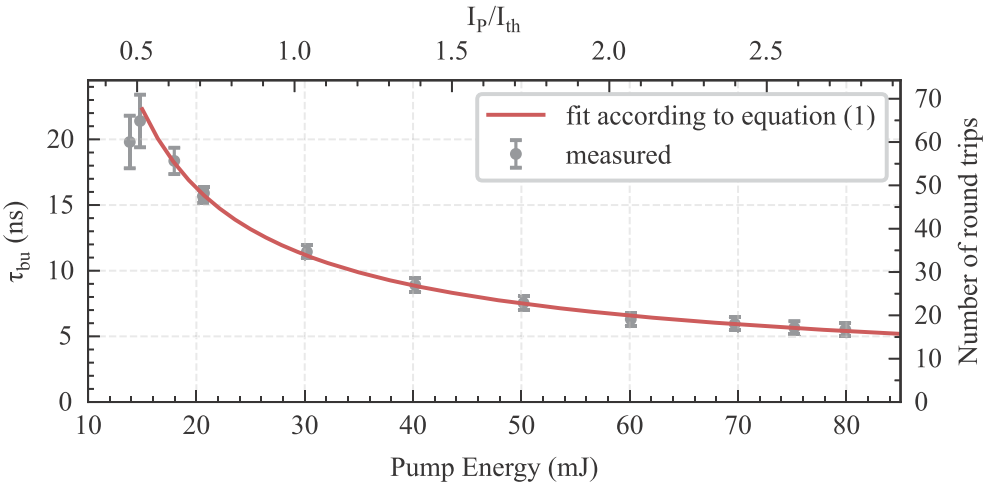

Fig. 4. Measured OPO build-up times, τ_{bu}, of the signal output vs. pump energy input. The number of cavity round trips is also indicated given a round trip time τ_{cav} = 0.31 ns. The red line represents a fit according to Eq. (1) for a value of the threshold pump energy E_{th} = 29 mJ. The alternate horizontal axis (top) indicates the normalized pump intensity I_p/I_{th} according to the intensity threshold I_{th} derived from the fitting procedure. Error bars are derived from shot-to-shot analysis.

[28,29]. The extracted ϵ = 0.42 is within the expected range and contains information on the effective reflectivity and other optical losses. For the E_{th} = 29 mJ obtained from the fit, the corresponding threshold intensity is I_{th} = 36 MW/cm^2, which is close to the characteristic irradiance of $I_{th,calc}$ = 38 MW/cm^2 that we calculated from the definition given in Refs. [16,30], for the signal and idler wavelengths and KTP crystal length. In Fig. 4, an alternate horizontal axis at the top is provided to indicate the normalized pump intensity I_p/I_{th} according to the intensity threshold I_{th} derived from the fitting procedure.

As expected, the OPO output is rather sensitive to the optical cavity alignment, as a result of interference between multiple cavity modes that can simultaneously be supported in an unstable resonator. The beating of these multiple modes can be observed from the oscilloscope traces for the OPO output as seen in the inset of Fig. 3. The measured beating period is 310 ps, which is close to the estimated cavity round trip time of 300 ps. Such beating dynamics has been anticipated in numerical studies [28,31] but has not been experimentally shown in the temporal domain, to the best of our knowledge. The further slow oscillations at ~ 8 ns period visible in both pump and OPO traces originate from the Agilite pump laser system.

Various measurements were performed to characterize and optimize the OPO for the highest output energies, optimal temporal profiles (considering build-up and temporal widths), and narrowest spectral widths (for mode stability, as discussed below). At these optimal conditions, the energy and beam pointing stability are also highest, providing an ideal starting point in seeding the MOPA amplification stage.

4. Optical parametric amplifier

4.1. Output energy

Figure 5(a) shows a graph of signal energies vs. varying OPA-pump pulse energies for the three different set pulse durations of the pump laser: 14 ns, 19 ns, and 27 ns. The pulse durations are altered by changing the timing of a Pockels cell within the pump laser to crop the box-shaped

Optics EXPRESS

laser pulse to the desired duration. Hence, the duration is changed without affecting the peak intensity and the overall shape of the laser pulse. To perform a scan of the pump pulse energy, a $\lambda/2$ wave-plate in combination with a thin-film polarizer is used. The intensity of the seed is kept constant at approximately 2 MW/cm^2, meaning that the seed energy is fixed at 1.3 mJ in the 14 ns setting, at 2 mJ in the 19 ns setting, and at 3 mJ in the 27 ns setting.

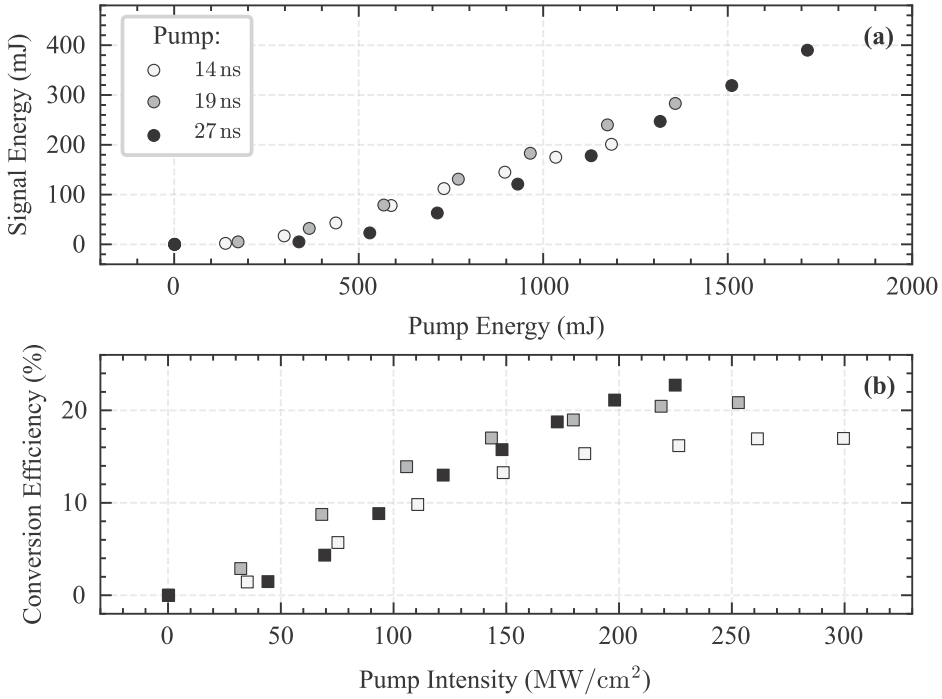

Fig. 5. (a) MOPA output, plotted as pulse energies at the signal wavelength of 2090 nm, as obtained by varying pump energies at three different pump pulse durations. (b) Conversion efficiencies for different pump intensities, again for the three different pump pulse durations. The conversion efficiency is defined as signal energy divided by pump energy. Error bars are smaller than the markers.

For pump energies E_{pump} ranging from 0 to 1.7 J used in the 27 ns setting, up to 390 mJ of signal energy is achieved, thus yielding an amplification factor of 130. Since idler and signal energies are similar, the total energy is estimated at 780 mJ. The corresponding maximum pump intensity is 220 MW/cm^2, calculated via $I = E_{\text{pump}}/(\tau\pi w^2)$ with the pump laser pulse duration τ = 27 ns and the laser beam radius w = FWHM/2 = 3.0 mm. Maximum pump intensities for the 19 ns and 14 ns settings are respectively 250 MW/cm^2 and 300 MW/cm^2, yielding signal (and, equivalently, idler) energies of up to 300 mJ and 200 mJ, respectively. Maximum pump intensities are limited by laser-induced damage thresholds of the antireflective coatings on the KTP crystal surfaces.

Figure 5(b) displays the conversion efficiency of pump energy to signal or idler energy for the OPA for varying pump intensities for the three different set pulse durations 14 ns, 19 ns, and 27 ns. The trends for all pulse duration settings follow the same pattern. The conversion efficiencies at 14 ns (CE_{14ns}) and at 19 ns (CE_{19ns}) settings show a plateauing behavior starting at pump intensities of 180 MW/cm^2. Here, the term saturation refers to this leveling of conversion efficiency at high pump intensities. CE_{14ns} saturates at 17 % and CE_{19ns} saturates with 20 % at a somewhat higher efficiency. CE_{27ns} does not reveal such a distinct saturation behavior and it reaches a total conversion efficiency of 22 % for the highest pump intensity. These differences in

Optics EXPRESS

saturation behavior might be explained by the varying temporal pulse shapes across the spatial profile of the pump beam (see section 4.3). This saturation of conversion efficiencies coincides with the transition of a non-linear increase of the signal/idler energies to a linear incline in Fig. 5(a), which is in line with the findings of Arisholm et al. [16]. The RMS deviation of the output energies at the highest pump intensity is 2.8% and increases to approximately 10% at the lowest pump intensities. This phenomenon may be ascribed to the effect of saturation.

It might be expected that higher output energies could be achieved by a further increase of the pump energy. However, for increased pump energies, laser-induced damage of the antireflective coatings on the KTP crystal surfaces is observed. Alternatively, more KTP crystals could be added to the OPA to enable operating at lower pump intensities. Additionally, dichroic mirrors could be used in between the KTP crystals of the OPA to reflect the idler beam out of the OPA. The latter would suppress nonlinear backconversion, although no direct evidence of such backconversion is observed. Filtering of the idler beam inside the OPA might be required, however, for increasing the efficiency at pump energies beyond 2 J, and for future power gains of high-energy pulsed KTP-based MOPA systems [16].

4.2. Spatial profiles

Figure 6 shows normalized spatial profiles of the seed beam, pump beam, and the signal beam generated by the MOPA at different pump intensities. The profiles at 2-µm wavelength are recorded using a pyroelectric camera (Ophir PyroCam IV), located at a fixed position approximately 3 m after the OPA. Using a single spherical lens, with a focal length of 600 mm, seed and MOPA beam profiles are imaged onto the chip of the pyroelectric camera with a magnification of 2.6×. The pump beam profile is taken using a silicon-based CCD camera (Ophir SP920) at a fixed position approximately 2 m after the OPA stage. Here, a spherical lens with a focal length of 300 mm is used to image the beam profile on the camera chip with a demagnification of 0.5×. All profiles in Fig. 6 share the same scaling factor and spatial coordinate grid to facilitate direct comparison.

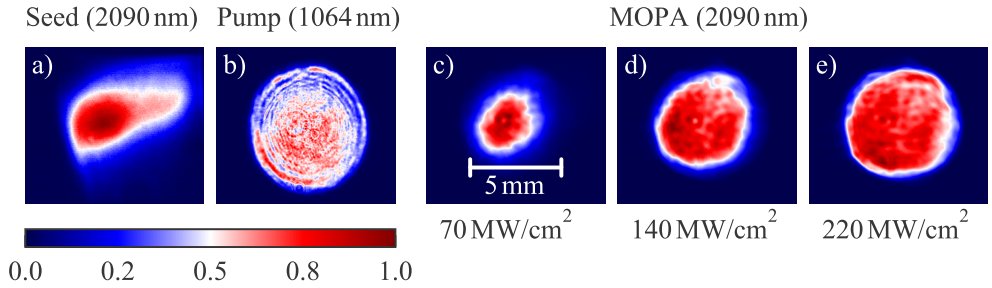

Fig. 6. Selection of beam profiles as imaged from a defined plane inside the OPA stage for the 27 ns pump pulse duration setting: (a) seed (signal) beam generated by the OPO with an FWHM of 5.3 × 2.3 mm^2. (b) flat-top pump beam profile with an FWHM of 6 mm. (c)-(e) show the amplified seed beam that is the output of the MOPA system, for different pump intensities. The flat-top beam profile generated at the highest pump intensity in panel (e) has an FWHM of 4.5 × 5.1 mm^2, and 85% of its total energy is enclosed within the FWHM contour. The OPO is for all cases pumped with a pump energy of 76 mJ at 27 ns pump-pulse duration.

Figure 6(a) shows the profile of the seed beam at 2090 nm, as it is transported from the OPO to the second crystal within the OPA, 300 mm after the OPO and twofold expanded, without relay imaging. The seed beam has an asymmetric shape, significantly different from that of the pump beam profile. This asymmetry may be caused by walk-off and by the multiple modes supported by the OPO cavity. Fig. 6(b) shows the beam profile of the pump within the OPA for a set pulse

Optics EXPRESS

duration of 27 ns. It resembles a flat-top beam distribution, with slight asymmetries characteristic to the pump-laser used. The fringes originate from the aperturing in the commercial Agilite laser system. The lower resolution of the pyroelectric camera is expected to significantly reduce the visibility of fringes in the signal beams (see below). Fig. 6(c–e) shows the signal beam of the MOPA for pump beam intensities of 70 MW/cm^2, 140 MW/cm^2, and 220 MW/cm^2. The diameter of the MOPA beam profile increases from 1.7×2.6 mm^2 to 4.5×5.1 mm^2 with increasing pump intensity. At the lowest pump intensity, the MOPA profile deviates mostly from a flat-top beam profile, following the seed beam profile. For increasing pump intensity, the MOPA beam profile gradually approaches a flat-top beam profile following the pump beam profile. The percentage of the energy enclosed inside the FWHM contour of the MOPA beam profile increases from approximately 50% to 85% at the highest pump intensity. Ring-like structures in the outer regime of the MOPA beam profiles become apparent, following similar features of the pump beam profile. The spatial flattening is explained by the fact that the local seed and pump intensities vary across the spatial overlap of the beam profiles. Consequently, the local parametric gain of the OPA depends on the position in the beam profile. In the center of the beam, the local gain is higher than at the edges, due to the peaking seed intensity at the beam center. This non-uniformity in the local gain affects the local conversion efficiency, which is the efficiency of converting pump energy to signal energy contained within a certain area of the beam profile. Consequently, the local conversion efficiency first saturates at the center. This leads to a flattening of the beam for increasing pump intensities when the outer areas of the beam profile catch up in local intensity and approach saturation at higher overall pump intensities. The MOPA beam profiles do not show definitive signs of backconversion such as local depletion in MOPA intensity caused by converting 2-µm light back to 1-µm light.

4.3. Temporal profiles

Figure 7 shows various characteristic temporal pulse profiles of the MOPA for a setting of the pump pulse to a box-shaped profile of 27 ns duration. The temporal pulse profiles of the pump beam before and after depletion in the OPA stage, the seed beam, and the amplified 2-µm wavelength after the MOPA (referred to as MOPA pulse) are displayed for three different pump intensities, being 220 MW/cm^2, 140 MW/cm^2 and 70 MW/cm^2. For an interpretation of the time axis, some synchronization technicalities should be considered. The pump pulse is optically delayed by approximately 4 ns before entering the OPA stage (see section 2.) resulting in a delay of about 1 ns between the onsets of the pump pulse and the seed and MOPA pulses. By delaying the pump pulse, the seed pulse becomes centered with respect to the pump pulse inside the OPA stage. This also causes the low-intensity parts of the seed pulse to experience maximum pump intensity, leading to a longer effective pulse duration (see Fig. 7).

The central result of these studies on temporal profiles is that a MOPA pulse can be generated exhibiting a box-shaped profile of 24 ns, as shown in Fig. 7, panel (a). Such a pattern can be achieved for a pump pulse of the highest intensity, at 220 MW/cm^2, that is also box-shaped. The box-shaped profile of the MOPA pulse is overlaid with a high-frequency oscillation, resulting from the longitudinal mode-beating pattern originating from the OPO seed (see Fig. 3). We note that the intensity at the beginning and end of the MOPA pulse inclines and declines more steeply than the intensity of the seed pulse. This behavior can be explained by a strongly non-linear, parametric amplification at lower seed intensities, whereas amplification is less strong at higher seed intensities due to saturation. The MOPA pulse increasingly deviates from the box shape of the pump pulse when moving to lower pump intensities, eventually becoming triangular in shape at the lowest intensities of 70 MW/cm^2. The measured pump profile after the OPA shows depletion of its energy in the form of a dip in the local pulse intensity at times coinciding with the MOPA pulse.

Optics EXPRESS

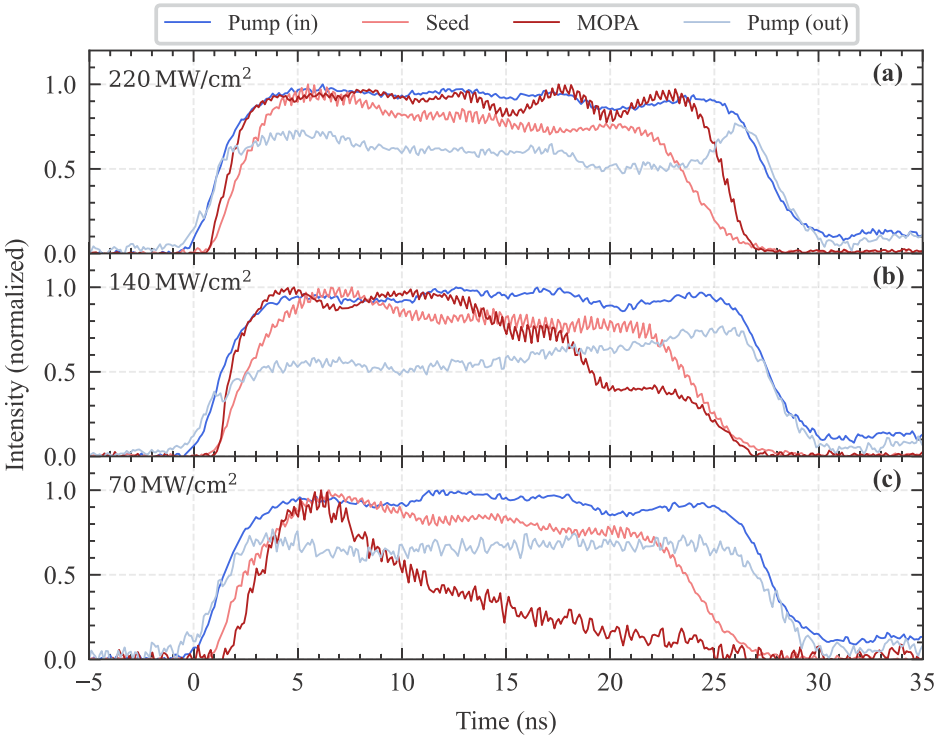

Fig. 7. (a)-(c) Temporal pulse profiles for a 27 ns pump pulse duration setting for pump intensities as specified in panels. The pulses of the initial pump, the seed, the MOPA output, and the depleted pump after amplification are presented. All but the depleted pump profile are normalized. The pulse profile of the depleted pump is scaled so that the integral matches the percentage of the remaining pump energy to visualize the effect of pump depletion. The light detected beyond 30 ns is assumed to originate from light leakage at the Pockels cells controlling the duration of the pump pulse.

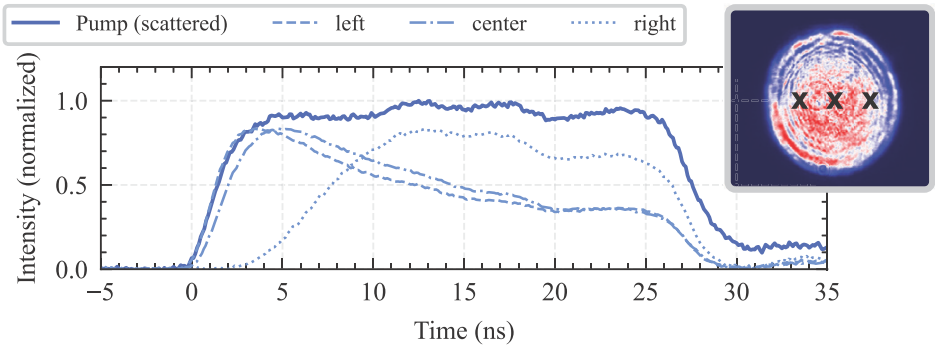

Fig. 8. Temporal profile of the pump pulse resolved across the spatial beam profile. The blue solid line shows the temporal trace of the scattered light, i.e. representative of the full beam. The dashed/dotted lines show traces recorded with a 200 µm pinhole mounted in front of a photodiode to obtain spatially resolved traces at left, center, and right locations as indicated in the inset figure.

Optics EXPRESS

In order to explain the temporal deformation of the MOPA pulse at lower pump intensities, the intensity of the incoming pump pulse is spatially probed using a photodiode equipped with a 200 µm pinhole in front. Results of this local probing are presented in Fig. 8, showing that the temporal shape of the pump pulse is triangular at the center and left-hand side of the beam. In contrast, on the right-hand side, it shows a slow increase followed by a plateau region. This behavior may be explained by considering that for the lowest pump intensities, the center of the seed spatial beam profile, where the intensity is highest, undergoes the strongest parametric amplification [cf. Fig. 6(a) and (c)]. So, only the part of the pump beam profile spatially overlapping with the center of the seed beam profile contributes significantly to the parametric amplification at lower pump intensities. As a result, the temporal MOPA pulse profile follows the pump pulse profile at the position of the peak of the seed beam profile; the shape is more triangular-like [cf. Fig. 8 and Fig. 7 (c)]. When the overall pump intensity increases, gradually more parts of the pump beam profile, overlapping with low-intensity areas of the seed beam profile, contribute to the parametric amplification, while the part with the highest seed intensity starts saturating in local conversion efficiency (as discussed in section 4.2). When summing up these spatially dependent temporal pulse profiles, the overall MOPA pulse will resemble the overall temporal shape of the pump pulse, forming a superposition of local, different, pulse shapes. Currently it is unclear if spatio-temporal coupling (STC) of the pump is translated onto any signal STC, nor is there a model available to predict the impact of STC on the generation of EUV-emitting plasma. Further study is required to clarify these new topics, enabled by the laser system presented in this work. Figure 9 shows temporal traces of the incoming pump pulse, the seed, the MOPA, and of the depleted pump, measured for different combinations of durations and

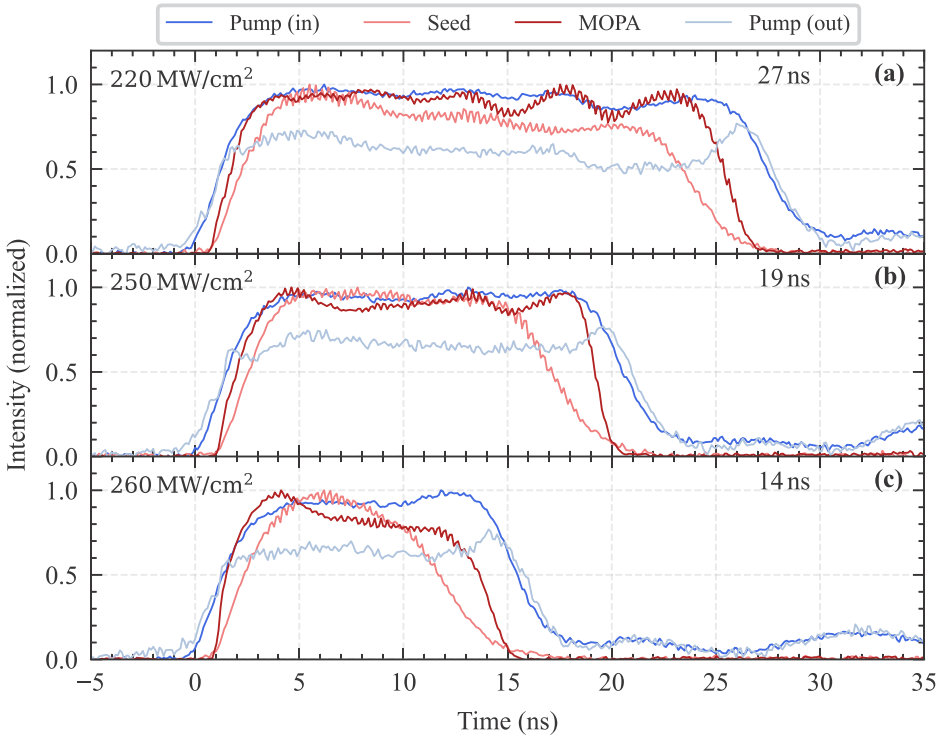

Fig. 9. Measured temporal profiles of the initial pump beam, the OPO-seed beam, and the MOPA signal beam, and the depleted pump are shown for settings of the pump pulse for combinations of duration and intensity as specified in the legends.

Optics EXPRESS

intensities of the pump pulse: 27 ns and 220 MW/cm^2, 19 ns and 250 MW/cm^2, and 14 ns and 260 MW/cm^2, respectively. The resulting durations of the MOPA pulses under these conditions are 24, 17, and 12 ns, respectively. At the high pump intensities, all exceeding 220 MW/cm^2, the temporal box-shaped pulses of the pump could be converted into box-shaped MOPA pulses. Interestingly, the difference between the durations of the pump pulses and the corresponding MOPA pulses is only 2–3 ns, whereas the difference between OPO-seed and pump pulse duration, i.e. the build-up time, is 5.5 ns (see Fig. 3). This phenomenon is attributed to the amplification of low-intensity parts on the side flanks of the seed pulse.

In conclusion, it is demonstrated that box-shaped temporal profiles of the MOPA pulses can be produced in a controlled fashion for varying pulse durations between 12 and 24 ns.

5. Spectrum and bandwidth

In this section, we discuss spectral measurements for the OPO output as well as the amplified MOPA output (for τ_p = 27 ns) recorded using a High-Finesse WS5 IR-III wavelength meter. Figure 10(a) shows OPO idler output spectra for different cavity alignment settings. The OPO idler wave, which has an orthogonal polarization to that of the signal wave, is separated by reflection from a thin film polarizer and is used for online monitoring, while the OPO signal wave output is transported towards the MOPA to seed the amplifier. At OPO cavity alignment-1, far from the output energy optimum, multiple spectral modes can be observed, which we attribute to multiple cavity modes simultaneously supported by the unstable resonator.

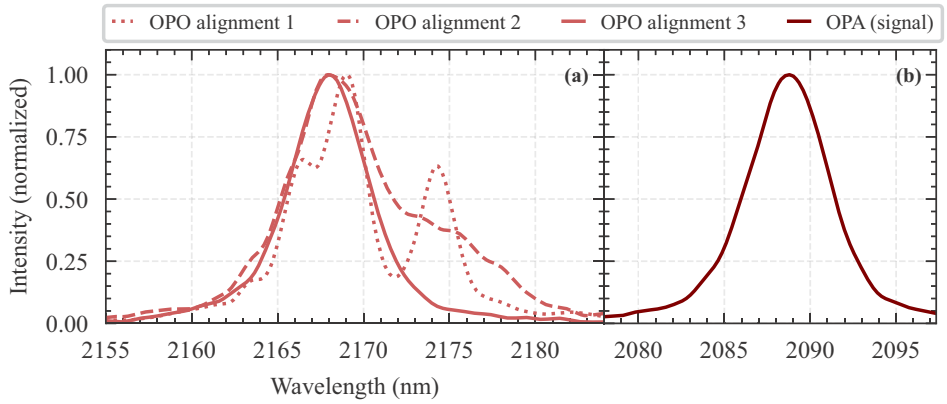

Fig. 10. (a) Spectral analysis of the OPO idler output wave for three different cavity alignment conditions. (b) Spectrum of the signal beam of the OPO alignment 3 in (a) after amplification in the MOPA stage.

The spectral FWHM width of each mode is 2.6 nm while the crystal acceptance bandwidth for OPO operation is estimated to be 4.7 nm from the nonlinear optics code SNLO [32]. (The instrument limit of the spectrometer is not exactly known at this wavelength, thus our measurement provides an upper limit.) The narrower linewidth for the observed individual modes may be due to gain narrowing effects, where nanosecond OPO linewidths can be as narrow as 20% of the crystal phase matching bandwidth [30]. The mode separation of 3 nm can be used to estimate the angular deviation of 0.8 mrad for neighboring cavity mode paths, which is easily supported considering the pump beam size and cavity length. As the cavity alignment is optimized towards higher output energy, the spectral profile becomes more uniform with fewer spectral modes (alignments-2 and -3), suggesting that the optimal alignment condition favors higher gains for a smaller number of modes. For optimum alignment conditions (OPO alignment-3), the highest

Optics EXPRESS

OPO output energy and narrowest composite spectral width are obtained, which also correlate with the highest energy- and spatial-beam profile stability.

In Fig. 10(b), the amplified signal wave spectra corresponding to OPO alignment-3 in Fig. 10(a) is shown. The OPA spectrum is taken when the amplifier is pumped with 1.7 J for a pump pulse duration of τ_p = 27 ns, corresponding to an intensity of 220 MW/cm^2. The FWHM width of the OPO alignment-3 spectrum in Fig. 10(a) is 5.0 nm, while the MOPA output FWHM width is marginally broader at 5.5 nm. The latter can be compared to the crystal phase-matching bandwidth for signal wave amplification in a single pass of 6.5 nm estimated using the SNLO code [32]. The SNLO code gives an OPO bandwidth that is narrower than the single-pass mixing bandwidth, with the same input parameters. It assumes that the signal and idler tune in equal amounts with respect to the fixed pump, hence it is the group velocity dispersion between signal and idler that is relevant. For amplification in the OPA, it is the dispersion of the group velocity between the seed (signal) and the pump that limits the phase matching. Note that for these spectral recordings, the OPO seed energy is about 1 mJ while the MOPA amplified output energy is around 400 mJ. The OPO and OPA spectral profiles demonstrate that even at high energy operation, the amplification process closely maintains the uniform and symmetric spectral characteristic of the seed radiation.

6. Conclusion

We built a parametric master oscillator power amplifier (MOPA) with an optical parametric oscillator (OPO) generating 2-µm wavelength light that is amplified by an optical parametric amplifier (OPA). This configuration allows for the generation of high-energy nanosecond pulses with a relatively good beam quality of $M^2 \approx 5$. The MOPA is pumped by a seeded 1064-nm Nd:YAG laser that has temporal pulse shaping capabilities. The MOPA can generate box-shaped temporal pulses with a tunable pulse duration from 10–24 ns. We demonstrate a total pulse energy of 800 mJ, signal and idler combined, from 2 J of pump energy input when using four KTP-crystals in the amplifier.

The total conversion efficiency of 1-µm to 2-µm wavelength light, combining signal and idler, saturates close to 44%. Close to the saturation level, the spatial beam profile of the MOPA follows the flat-top shape of the pump beam. We find a similar behavior in the temporal domain, where the output pulse approaches a box-shaped temporal profile comparable to the input pump pulse for increasing pump intensities. The flat-top spatial and box-shaped temporal profiles are realized due to saturation effects of the conversion efficiency in the OPA stage.

Even at the highest output energies, the beam divergence is sufficient for imaging the beam to a highly intense flat-top profile below 100 µm diameter. Certain EUV plasma studies require highly energetic pulsed laser radiation to irradiate a sub-100 µm micro-droplet tin target with high intensities. Those high pulse energies are not only restricted to 2-µm wavelength since the output wavelength of a MOPA can in principle be tuned in a range from 1.4–3 µm by changing the phase-matching angle of the KTP crystals. Hence, our MOPA is an ideal laser source for EUV plasma studies and applications that require high pulse energies at good beam qualities in the mid-infrared range.

Funding. HORIZON EUROPE European Research Council (ERC StG 802648); Nederlandse Organisatie voor Wetenschappelijk Onderzoek (OTP 19458, Vidi 15697).

Acknowledgments. This work has been carried out at the Advanced Research Center for Nanolithography (ARCNL). ARCNL is a public-private partnership with founding partners UvA, VU, NWO-I and ASML, and associate partner RUG.

Disclosures. The authors declare no conflicts of interest.

Data availability. Data underlying the results presented in this paper are not publicly available at this time but may be obtained from the authors upon reasonable request.

Optics EXPRESS

References

1. F. K. Tittel, D. Richter, and A. Fried, *Mid-Infrared Laser Applications in Spectroscopy* (Springer Berlin Heidelberg, Berlin, Heidelberg, 2003), pp. 458–529.
2. T. Wagener, N. Demma, J. Kmetec, and T. Kubo, "2 μm LIDAR for laser-based remote sensing: flight demonstration and application survey," IEEE Aerosp. Electron. Syst. Mag. **10**(2), 574–579 (1995).
3. V. Serebryakov, E. Boiko, N. Petrishchev, and A. Yan, "Medical applications of mid-IR lasers. Problems and prospects," J. Opt. Technol. **77**(1), 6–17 (2010).
4. V. Petrov, "Parametric down-conversion devices: The coverage of the mid-infrared spectral range by solid-state laser sources," Opt. Mater. **34**(3), 536–554 (2012).
5. A. Godard, "Infrared (2–12 μm) solid-state laser sources: a review," C. R. Phys. **8**(10), 1100–1128 (2007).
6. J. Ma, Z. Qin, G. Xie, L. Qian, and D. Tang, "Review of mid-infrared mode-locked laser sources in the 2.0 μm–3.5 μm spectral region," Appl. Phys. Rev. **6**(2), 021317 (2019).
7. L. Behnke, R. Schupp, Z. Bouza, M. Bayraktar, Z. Mazzotta, R. Meijer, J. Sheil, S. Witte, W. Ubachs, R. Hoekstra, and O. O. Versolato, "Extreme ultraviolet light from a tin plasma driven by a 2-μm-wavelength laser," Opt. Express **29**(3), 4475–4487 (2021).
8. R. Schupp, F. Torretti, R. Meijer, M. Bayraktar, J. Scheers, D. Kurilovich, A. Bayerle, K. Eikema, S. Witte, W. Ubachs, R. Hoekstra, and O. O. Versolato, "Efficient Generation of Extreme Ultraviolet Light From Nd:YAG-Driven Microdroplet-Tin Plasma," Phys. Rev. Appl. **12**(1), 014010 (2019).
9. C. N. Danson, C. Haefner, and J. Bromage, *et al.*, "Petawatt and exawatt class lasers worldwide," High Power Laser Sci. Eng. **7**, e54 (2019).
10. E. Sistrunk, D. A. Alessi, A. Bayramian, K. Chesnut, A. Erlandson, T. C. Galvin, D. Gibson, H. Nguyen, B. Reagan, K. Schaffers, C. W. Siders, T. Spinka, and C. Haefner, "Laser Technology Development for High Peak Power Lasers Achieving Kilowatt Average Power and Beyond," Proc. SPIE **11034**, 1103407 (2019).
11. I. Tamer, B. A. Reagan, T. Galvin, J. Galbraith, E. Sistrunk, A. Church, G. Huete, H. Neurath, and T. Spinka, "Demonstration of a compact, multi-joule, diode-pumped Tm:YLF laser," Opt. Lett. **46**(20), 5096–5099 (2021).
12. I. Tamer, B. A. Reagan, T. Galvin, F. Batysta, E. Sistrunk, D. Willard, A. Church, H. Neurath, J. Galbraith, G. Huete, and T. Spinka, "1 GW peak power and 100 J pulsed operation of a diode-pumped Tm:YLF laser," Opt. Express **30**(26), 46336–46343 (2022).
13. G. A. Rines, D. M. Rines, and P. F. Moulton, "Efficient, high-energy, KTP optical parametric oscillators pumped with 1 micron Nd-lasers," in *Advanced Solid State Lasers*, (Optica Publishing Group, 1994), p. PO9.
14. M. S. Webb, P. F. Moulton, J. J. Kasinski, R. L. Burnham, G. Loiacono, and R. Stolzenberger, "High-average-power $KTiOAsO_4$ optical parametric oscillator," Opt. Lett. **23**(15), 1161–1163 (1998).
15. A. V. Smith and M. S. Bowers, "Image-rotating cavity designs for improved beam quality in nanosecond optical parametric oscillators," J. Opt. Soc. Am. B **18**(5), 706–713 (2001).
16. G. Arisholm, O. Nordseth, and G. Rustad, "Optical parametric master oscillator and power amplifier for efficient conversion of high-energy pulses with high beam quality," Opt. Express **12**(18), 4189–4197 (2004).
17. B. C. Johnson, V. J. Newell, J. B. Clark, and E. S. McPhee, "Narrow-bandwidth low-divergence optical parametric oscillator for nonlinear frequency-conversion applications," J. Opt. Soc. Am. B **12**(11), 2122–2127 (1995).
18. W. A. Neuman and S. P. Velsko, "Effect of cavity design on optical parametric oscillator performance," in *Advanced Solid State Lasers*, (Optica Publishing Group, 1996), p. OP12.
19. J. N. Farmer, M. S. Bowers, and W. S. Scharpf, "High brightness eyesafe optical parametric oscillator using confocal unstable resonators," in *Advanced Solid State Lasers*, (Optica Publishing Group, 1999), p. WC2.
20. S. Haidar and H. Ito, "Injection-seeded optical parametric oscillator for efficient difference frequency generation in mid-IR," Opt. Commun. **171**(1-3), 171–176 (1999).
21. Y. Ehrlich, S. Pearl, and S. Fastig, "High brightness tunable tandem optical parametric oscillator at 8-12 μm," in *Advanced Solid-State Photonics (TOPS)*, (Optica Publishing Group, 2004), p. 398.
22. D. J. Armstrong and A. V. Smith, "Demonstration of improved beam quality in an image-rotating optical parametric oscillator," Opt. Lett. **27**(1), 40–42 (2002).
23. A. V. Smith and D. J. Armstrong, "Nanosecond optical parametric oscillator with 90° image rotation: design and performance," J. Opt. Soc. Am. B **19**(8), 1801–1814 (2002).
24. W. R. Bosenberg and D. R. Guyer, "Broadly tunable, single-frequency optical parametric frequency-conversion system," J. Opt. Soc. Am. B **10**(9), 1716–1722 (1993).
25. J. C. McCarthy, R. C. Day, and E. P. Chicklis, "Novel, efficient, high brightness KTP optical parametric oscillator - amplifier in single beamline," in *Advanced Solid-State Lasers*, (Optica Publishing Group, 2001), p. WD4.
26. R. Schupp, L. Behnke, J. Sheil, Z. Bouza, M. Bayraktar, W. Ubachs, R. Hoekstra, and O. O. Versolato, "Characterization of 1- and 2-μm-wavelength laser-produced microdroplet-tin plasma for generating extreme-ultraviolet light," Phys. Rev. Res. **3**(1), 013294 (2021).
27. R. Schupp, L. Behnke, Z. Bouza, Z. Mazzotta, Y. Mostafa, A. Lassise, L. Poirier, J. Sheil, M. Bayraktar, W. Ubachs, and O. O. Versolato, "Characterization of angularly resolved EUV emission from 2-μm-wavelength laser-driven Sn plasmas using preformed liquid disk targets," J. Phys. D: Appl. Phys. **54**(36), 365103 (2021).
28. A. Godard, M. Guionie, J.-B. Dherbecourt, J.-M. Melkonian, and M. Raybaut, "Backward optical parametric oscillator threshold and linewidth studies," J. Opt. Soc. Am. B **39**(2), 408–420 (2022).

Optics EXPRESS

29. G. Arisholm, R. Paschotta, and T. Südmeyer, "Limits to the power scalability of high-gain optical parametric amplifiers," J. Opt. Soc. Am. B **21**(3), 578–590 (2004).
30. A. V. Smith, *Crystal nonlinear optics: with SNLO examples* (AS-Photonics, Albuquerque, NM, USA, 2018).
31. A. V. Smith, R. J. Gehr, and M. S. Bowers, "Numerical models of broad-bandwidth nanosecond optical parametric oscillators," J. Opt. Soc. Am. B **16**(4), 609–619 (1999).
32. A. V. Smith, AS-Photonics, "SNLO nonlinear optics code," https://as-photonics.com/products/snlo/ (2023).